



## 3-D coseismic displacement mapping of the 2015 Mw7.8 Gorkha earthquake using multi-viewed InSAR

Han Chen <sup>a</sup>, Chunyan Qu <sup>a,\*</sup>, Dezheng Zhao <sup>b</sup>, Xinjian Shan <sup>a</sup>, Chao Ma <sup>c</sup>, Wenyu Gong <sup>a</sup>, Lei Zhao <sup>d</sup>, Luca Dal Zilio <sup>e,f</sup>

<sup>a</sup> State Key Laboratory of Earthquake Dynamics, Institute of Geology, China Earthquake Administration, Beijing 100029, China

<sup>b</sup> State Key Laboratory for Mineral Deposits Research, School of Earth Sciences and Engineering, Nanjing University, Nanjing 210023, China

<sup>c</sup> School of Surveying and Land Information Engineering, Henan Polytechnic University, Jiaozuo 454003, China

<sup>d</sup> Key Laboratory of Metallogenic Prediction of Nonferrous Metals and Geological Environment Monitoring, Central South University, Ministry of Education, Changsha 410000, China

<sup>e</sup> Institute of Geophysics, Department of Earth Sciences, ETH Zürich, Zürich, Switzerland

<sup>f</sup> Earth Observatory of Singapore, Nanyang Technological University, Singapore

### ARTICLE INFO

#### Keywords:

Gorkha earthquake  
InSAR  
Offset-tracking  
3-D displacement fields  
Strain map  
Earthquake cycle

### ABSTRACT

After the 2015 Mw7.8 Gorkha earthquake, geodetic measurements have been extensively used to constrain slip kinematics, fault geometry of the Main Himalayan Thrust (MHT) and earthquake cycle deformation. However, the spatially dense coseismic 3-D displacements remain largely unresolved, owing to the side-looking geometry of SAR images and sparse GPS observations. We improved 3-D displacements by incorporating a strain model in a Bayesian framework, utilizing all available coseismic interferograms and azimuth offsets from Sentinel-1 and ALOS-2 satellites. The coseismic strain map shows that major landslides in large slope areas are spatially consistent with extensional strain. The vertical component illustrates a spatial pattern different from interseismic and postseismic uplift, hinting at diverse contributions from various tectonic uplift processes in the frontal mountain belt. The spatial relationship between the interseismic strain and coseismic deformation suggests a partial release of the accumulated strain, implying a remaining notable seismic hazard around Gorkha.

### 1. Introduction

The Himalayan orogenic belt is one of the most seismically active regions worldwide due to the rapid convergence (~40 mm/yr) and the continuous collision of the India-Eurasia plates (e.g., Avouac, 2015; Bilham, 2019; Dal Zilio et al., 2021). Seismicity is concentrated in a narrow ~50–70 km band across the Main Himalayan Thrust (MHT), a large-scale, north-dipping décollement representing the interseismically locked portion of the MHT (Fig. 1; e.g., Dal Zilio et al., 2020). At least eight great earthquakes of Mw > 7.5 are known to have occurred in history along the MHT (Fig. 1), but still leaving several seismic gaps with a high potential of major or great earthquakes. Understanding the mechanisms of strain accumulation and the relationship between megathrust earthquakes and mountain building are essential in earthquake hazard assessments.

The 2015 Mw 7.8 Gorkha earthquake partially ruptured the locked portions of the MHT near Kathmandu, but did not break the surface. This

likely indicates highly heterogeneous pre-seismic stress or substantial relict heterogeneous strain inherited from previous earthquakes (Avouac et al., 2015; Bilham, 2019; Elliott et al., 2016; Mencin et al., 2016). The Gorkha earthquake was the largest along the Himalayan arc since the 1950 Mw 8.6 Assam-Tibet earthquake in Nepal (Elliott et al., 2016) with the record of large-volume Sentinel-1 SAR images. Hence, the Gorkha earthquake provides a unique opportunity to investigate the deformation characteristics of megathrust earthquakes and their role in building the Himalaya Mountains.

The significant coseismic deformation and subsequent time-dependent postseismic deformation have been extensively investigated and well documented by geodetic measurements (InSAR/GPS; e.g., Ingleby et al., 2020; Lindsey et al., 2015; Liu-Zeng et al., 2020; Wang and Fialko, 2018; Zhao et al., 2017). Ample coseismic deformation measurements provide robust geodetic constraints on the fault geometry of the MHT (e.g., Ingleby et al., 2020), dynamic rupture processes (e.g., Yue et al., 2017) and fault slip distributions (e.g., Qiu et al., 2016; Feng

\* Corresponding author.

E-mail address: [dqyquchy@163.com](mailto:dqyquchy@163.com) (C. Qu).

et al., 2015; Dal Zilio et al., 2019).

Previous studies have examined the 3D displacements associated with the Gorkha earthquake (e.g., Elliott et al., 2016; Qu et al., 2020). However, previous studies have primarily relied on D-InSAR coseismic displacements. Due to the nearly north-south flight direction and side-looking imaging geometry of SAR satellites, D-InSAR interferograms are inherently less sensitive to north-south components of crustal deformation. To mitigate such limitations, previous studies have attempted to model the coseismic north-south displacements by inverting coseismic displacements. However, those results are heavily dependent on the unresolved geometry of the MHT (e.g., Wang and Fialko, 2015; Elliott et al., 2016; Mendoza et al., 2019). In addition, a rigid layer or significant lateral variation can also have an effect on the deformation modeling (Wang et al., 2024). To address these challenges and to provide a more comprehensive understanding of the 3D displacements, we utilized both D-InSAR interferograms and azimuth observations to better resolve the 3D displacements in this study. Azimuth observations, which can provide valuable constraints on the north-south component, are fully available for this earthquake based on previous studies (e.g., Liang and Fielding, 2017; Yue et al., 2017). By combining

multiple datasets, we obtained a more reliable 3D deformation field.

The vertical displacement contains important information regarding the relationship between coseismic uplift/subsidence and topographic evolution. The coseismic uplift could be compared to the long-term mountain building (e.g., Dal Zilio et al., 2021; Grandin et al., 2012), which provokes distinct mechanisms for the building of the Himalayan Mountains (e.g., Elliott et al., 2016; Whipple et al., 2016). Horizontal displacement could be utilized to derive the distribution of coseismic finite strain, which may control the distribution of locally triggered landslides (e.g., Chuang et al., 2020). Despite the recognized limited landslides triggered by the Gorkha earthquake (e.g., Xu et al., 2016), the relationship between the landslides and the horizontal strain (extension/contraction) is unclear.

In this study, we refine our understanding of the full 3-D displacement of the 2015 Gorkha earthquake by utilizing D-InSAR interferograms and azimuth offset measurements. We extend the proposed approach in Liu et al. (2018) by integrating a strain model in a Bayesian framework, which could better reconstruct north-south displacements for multi-viewed InSAR observations compared to traditional methods. We examine the spatial relationship between the horizontal

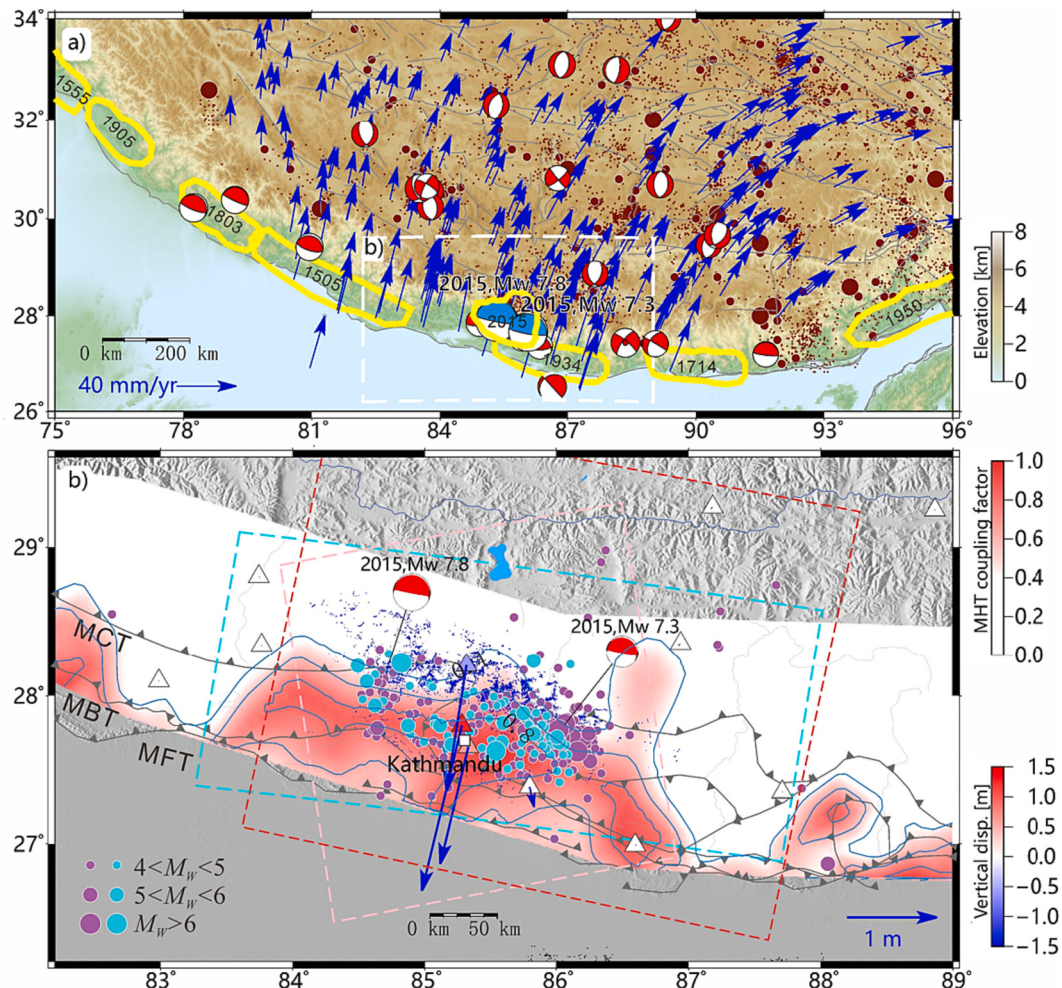


**Fig. 1.** Tectonic setting of the 2015 Gorkha earthquake. (a) Interseismic GPS velocities in the Eurasia-fixed reference frame (blue arrows, Wang and Shen, 2020) and historic earthquakes denoted by yellow polygons showing the approximate extent of major and great historical earthquakes along the Main Himalayan Thrust (MHT, Bilham, 2019). Brown dots indicate the historical seismicity ( $M_w > 2$ ) before the Gorkha earthquake from the China Earthquake Networks Center (CENC) catalog. (b) Degree of interseismic locking along the central Himalaya. Light blue contours illustrate a 0.2 interval of the coupling factor ( $\geq 0.4$ ) (Dal Zilio et al., 2020). Blue dots indicate the coseismically triggered landslides (Roback et al., 2018). Blue-to-red colored triangles represent vertical GPS coseismic displacements and blue arrows show horizontal displacements (Wang and Fialko, 2015). Pink and cyan boxes show the coverage of Sentinel-1 SAR images. Red boxes show the coverage of ALOS-2 SAR images. Light blue circles indicate aftershocks on April 25, 2020, and the purple ones denote aftershocks after April 25, 2020. Focal mechanisms ( $M_w > 6$ ) are from the Global CMT catalog (see Data and Resources). (For interpretation of the references to colour in this figure legend, the reader is referred to the web version of this article.)

displacement (strain) and the landslides. We investigate the locations and patterns of coseismic uplift, which is subsequently compared to other tectonic uplift processes in the earthquake cycle.

## 2. Data and methods

### 2.1. InSAR data and processing

We process interferometric pairs of radar images from the Sentinel-1 A satellite on ascending (T85) and descending tracks (T19 and T121) and from the ALOS-2 satellite on descending track (ScanSAR data, T48) to measure the coseismic deformation of the Gorkha earthquake. Detailed parameters of SAR images are listed in **Table S1**. The detailed methodology for interferogram formation is described in **Text S1** of the supplementary information.

### 2.2. Azimuth measurements from offset-tracking

Azimuth offsets provide important constraints on the north-south displacements in 3-D decomposing. We therefore compute the azimuth offsets using the subpixel offset-tracking algorithm, implemented in GAMMA (Strozzi et al., 2002; Werner et al., 2005), to ascending and descending Sentinel-1 SAR amplitude images.

We estimate azimuth offsets between two full-resolution amplitude images. The size of the correlation matching window is 200 pixels  $\times$  40 pixels in range and azimuth, respectively. In this way, an almost squared area is considered. Steps are 100 pixels in range and 20 pixels in azimuth. To improve the sampling of the used correlation function, the oversampling ratio of 2 is adopted (Werner et al., 2005). Mismatches and errors during offset-tracking are masked using a threshold ( $<0.1$ ) of the correlation coefficient, and further removed using a Gaussian low-pass filter, effectively tackling speckle noises. The precision of resultant azimuth offsets is approximately 1/30 of the image resolution (Werner et al., 2005; Mahmoud et al., 2020), corresponding to  $\sim 0.75$  m for Sentinel-1 SAR images with a  $\sim 22.5$  m azimuth resolution (e.g., Yagtie-Martínez et al., 2016), which is smaller than the observed 2–3 m azimuth offsets from ALOS-2 and RADARSAT-2 data (e.g., Liang and Fielding, 2017; Yue et al., 2017).

We also compile the surface displacements in the azimuth direction from the ALOS-2 data on the descending track (T48, see Fig. 2g), which is processed by Liang and Fielding (2017) using the multiple aperture InSAR (MAI) method.

### 2.3. 3-D displacement decomposing

The D-InSAR measurements are limited to the line-of-sight (LOS)

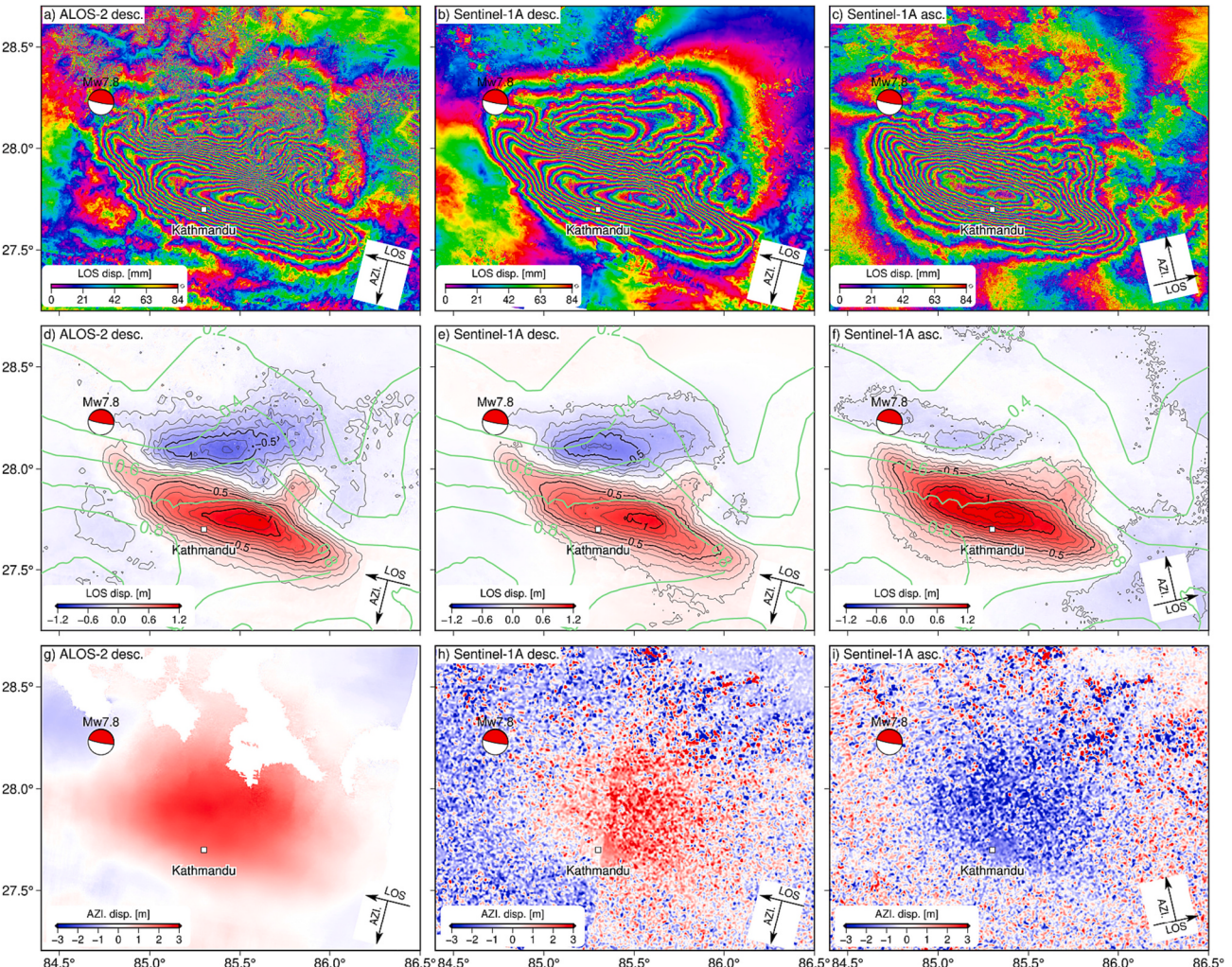


**Fig. 2.** (a, b, c) Coseismic line-of-sight (LOS) interferograms, (d, e, f) LOS displacement fields, and (g, h, i) azimuth offsets of the 2015 Gorkha earthquake derived from ALOS-2 and Sentinel-1 SAR data. Red beachball indicates the focal mechanism of the 2015 Gorkha earthquake. Light green contours in (d, e, f) illustrate a 0.2 interval of the interseismic coupling factor (based on Dal Zilio et al., 2020). (For interpretation of the references to colour in this figure legend, the reader is referred to the web version of this article.)

direction because of its side-looking geometry (e.g., Hu et al., 2014; Liu et al., 2018). Technically reconstructing 3-D displacements can be achieved by combining multiple InSAR observing geometries (e.g., Wright et al., 2004) or by combining InSAR and GPS observations (e.g., Gudmundsson et al., 2002). Here, we draw on six observations, three LOS displacement measurements and three azimuth offset measurements, from ascending and descending Sentinel-1 tracks and a descending ALOS-2 track to decompose full 3-D coseismic displacements. The addition of the azimuth offset measurements help to better constrain the north-south component of 3-D displacements.

The thrusting motion during the 2015 Gorkha earthquake caused large north-south and vertical displacements, while the north-south displacements provided a negligible contribution to the observed displacements in the LOS direction compared to the vertical component. Accurately reconstructing the north-south displacement requires multi-viewed InSAR LOS and azimuth observations, as well as an advanced algorithm that could robustly resolve the north-south component (e.g., Gudmundsson et al., 2002; Hu et al., 2014; Liu et al., 2018). To this end, we follow the strain-based approach proposed by Liu et al. (2018) to compute 3-D displacements of the 2015 Gorkha earthquake. This method incorporates a strain model to describe the spatial correlation of 3-D displacements between the adjacent points at the surface. The mathematical relationship between the 3-D displacement components of the interested point ( $d_e, d_n, d_u$ ) and the observation vectors of the adjacent points ( $D_{obs}^i$ ) can be described as follows:

$$D_{obs}^i = \begin{bmatrix} LOS_{asc}^i \\ AZI_{asc}^i \\ LOS_{desc}^i \\ AZI_{desc}^i \\ LOS_{alos}^i \\ AZI_{alos}^i \end{bmatrix} = [B_{geo}^i] \cdot [B_{sm}^i] \cdot [d_e \ d_n \ d_u \ \xi_{11} \ \xi_{12} \ \xi_{13} \ \xi_{22} \ \xi_{23} \ \xi_{33} \ \omega_1 \ \omega_2 \ \omega_3]^T$$

in which  $B_{geo}^i$  and  $B_{sm}^i$  can be expressed as:

$$B_{geo}^i = \begin{bmatrix} -\sin\theta_{asc}^i \sin\left(\alpha_{asc}^i - \frac{3\pi}{2}\right) & -\sin\theta_{asc}^i \cos\left(\alpha_{asc}^i - \frac{3\pi}{2}\right) & \cos\theta_{asc}^i \\ -\cos\left(\alpha_{asc}^i - \frac{3\pi}{2}\right) & \sin\left(\alpha_{asc}^i - \frac{3\pi}{2}\right) & 0 \\ -\sin\theta_{desc}^i \sin\left(\alpha_{desc}^i - \frac{3\pi}{2}\right) & -\sin\theta_{desc}^i \cos\left(\alpha_{desc}^i - \frac{3\pi}{2}\right) & \cos\theta_{desc}^i \\ -\cos\left(\alpha_{desc}^i - \frac{3\pi}{2}\right) & \sin\left(\alpha_{desc}^i - \frac{3\pi}{2}\right) & 0 \\ -\sin\theta_{alos}^i \sin\left(\alpha_{alos}^i - \frac{3\pi}{2}\right) & -\sin\theta_{alos}^i \cos\left(\alpha_{alos}^i - \frac{3\pi}{2}\right) & \cos\theta_{alos}^i \\ -\cos\left(\alpha_{alos}^i - \frac{3\pi}{2}\right) & \sin\left(\alpha_{alos}^i - \frac{3\pi}{2}\right) & 0 \end{bmatrix}$$

$$B_{sm}^i = \begin{bmatrix} 1 & 0 & 0 & \Delta x^i & \Delta y^i & \Delta z^i & 0 & 0 & 0 & 0 & \Delta z^i & -\Delta y^i \\ 0 & 1 & 0 & 0 & \Delta x^i & 0 & \Delta y^i & \Delta z^i & 0 & -\Delta z^i & 0 & \Delta x^i \\ 0 & 0 & 1 & 0 & 0 & \Delta x^i & 0 & \Delta y^i & \Delta z^i & \Delta y^i & -\Delta x^i & 0 \end{bmatrix}$$

where  $\Delta x^i, \Delta y^i, \Delta z^i$  are the increment of coordinates between the point of interest and the surrounding points;  $\alpha$  is the heading angle of the satellite;  $\theta$  is the incidence angle for a specific pixel.

We apply a Bayesian algorithm developed by Goodman and Weare (2010) with a Markov Chain Monte Carlo (MCMC) sampler to determine the best-fitting values for model parameters ( $d_e, d_n, d_u, \xi_{11}, \xi_{12}, \xi_{13}, \xi_{22}, \xi_{23}, \xi_{33}, \omega_1, \omega_2, \omega_3$ ,

$\xi_{33}, \omega_1, \omega_2, \omega_3$ ) and to account for their full uncertainties. This algorithm permits calculations of the full covariance of the unknown parameters and accounts for potential trade-offs between them. Initially, we adopt 700 initial walkers, representing different points in the parameter space, denoted as  $m_i = (d_e^i, d_n^i, d_u^i, \xi_{11}^i, \xi_{12}^i, \xi_{13}^i, \xi_{22}^i, \xi_{23}^i, \xi_{33}^i, \omega_1^i, \omega_2^i, \omega_3^i)$ . These starting points are derived from Gaussian distributions centered around values informed by the strain model, ensuring a broad and diverse coverage of the parameter space. Our method for each pixel runs over 1,000,000 iterations, and each walker independently explores the parameter space. In each iteration, we propose new parameter values for the walkers, based on a balance between their current positions and those of others. In this process, the step size is set to 2.5, ensuring comprehensive exploration of the full parameter space and efficient sampling. The acceptance of each new proposed set of parameters is determined by evaluating the likelihood function  $f(m)$ , in conjunction with the prior distribution. We assume a uniform prior for all unknown parameters with specific constraints on their possible values based on geophysical studies ( $-5 \leq d_e, d_u \leq 5$ ,  $-10 \leq d_n \leq 5$ , and  $-20$  to  $20$  for other parameters). This combination of likelihood and prior assessments allows for a probabilistic exploration of the parameter space, guiding the walkers toward regions of higher probability. The likelihood function  $f(m)$ , is formulated as follows:

$$f(m) = \sum \left( -\frac{1}{2} \left( \frac{L - l}{e^{\log(\sigma)}} \right)^2 - \log\left(\sqrt{2\pi} \cdot \log(\sigma)\right) \right)$$

Here the  $L$  represents the observed values, and  $l$  denotes the predictions of the model, which are functions of the model parameters  $m$ . The term  $\sigma$  is the standard deviation of the residuals between the model and the observations.

The first 20% of the iterations are discarded as burn-in to ensure that the samples used for inference are not influenced by the initial conditions. The remaining iterations provide a robust sample from which we can infer the posterior distributions of our model parameters. These distributions capture the uncertainties and correlations of the parameter space. Finally, we obtain both a posteriori probability density functions and related uncertainties. We prefer the maximum a posteriori solution as the most representative value for each parameter (Figs. S6, S7).

### 3. Results

#### 3.1. Coseismic LOS displacement fields and azimuth offsets

We illustrate our calculated and compiled LOS displacement measurements and azimuth offsets from Sentinel-1 and ALOS-2 data in Fig. 2. The LOS displacement fields observed from three distinct tracks exhibit a similar pattern, featuring an uplifted zone in the southern region and a subsiding zone in the northern region. Such a similar pattern along ascending and descending tracks indicates that the coseismic deformation is dominantly contributed by the coseismic vertical deformation. The maximum uplift observed in the southern zone is estimated to be  $\sim 1.1$  m, while the maximum subsidence in the northern zone is  $\sim 0.7$  m. The amplitude, distribution and pattern of the coseismic deformation in the LOS direction are consistent with previous studies (e.g., Elliott et al., 2016; Sreejith et al., 2016; Tung and Masterlark, 2016; Qu et al., 2020). The derived azimuth offsets on the descending Sentinel-1 track (Fig. 2h) are also similar to previous studies (Liang and Fielding, 2017; Yue et al., 2017) but with a higher noise level, with a peak value of  $\sim 2\text{--}3$  m, and has an opposite sign to ascending measurements (Fig. 2i). The sharp displacement boundary of the azimuth offset result (Fig. 2h) is the boundary between different frames. The Sentinel-1 offset measurements (Fig. 2h, i) exhibit higher noise levels than ALOS-2 azimuth offsets (Fig. 2g; Liang and Fielding, 2017), because the precision of offset measurements partly depends on the coherence of SAR image pairs (Bamler and Eineder, 2005). The L-band ALOS-2 data have better

coherence than C-band Sentinel-1 data in the case of the Gorkha earthquake.

Prior to the integration of azimuth offsets with LOS measurements, we test the influence of filter strength, denoted by the window size of the Gaussian averaging filter, on the noise reduction and the final deformation pattern of Sentinel-1 azimuth offsets. The results of this test are shown in Fig. S1. Overall, increasing the filter strength from 25 to 100 pixels gives rise to an anticipated trade-off between decreasing noise level and increasing deformation smoothness. To avoid erroneously reducing the azimuth offset amplitude during the filtering by averaging good pixel offset-tracking matches with bad matches, we adopt a filter strength (25 pixels) to achieve appropriate noise reduction and

smoothed displacement patterns (Fig. 2h, i).

The precision of offset tracking is also influenced by the size of the matching window (e.g., Bamler and Eineder, 2005). To understand such an effect, we conducted additional tests for offset tracking results along the ascending track with varied dimensions of matching windows, ranging from  $250 \times 50$  to  $128 \times 64$  in range  $\times$  azimuth. We calculated the mean azimuth offsets for all matching windows (range  $\times$  azimuth:  $250 \times 50$ ,  $200 \times 40$ ,  $150 \times 30$ ,  $256 \times 128$ ,  $128 \times 64$ ) and the corresponding standard deviations (Fig. S2). Our findings, using a fixed Gaussian filter strength of 25 pixels, reveal that the azimuth offsets determined using a matching window,  $200 \times 40$  (Fig. 2i), display a striking similarity to the averaged results derived from various matching

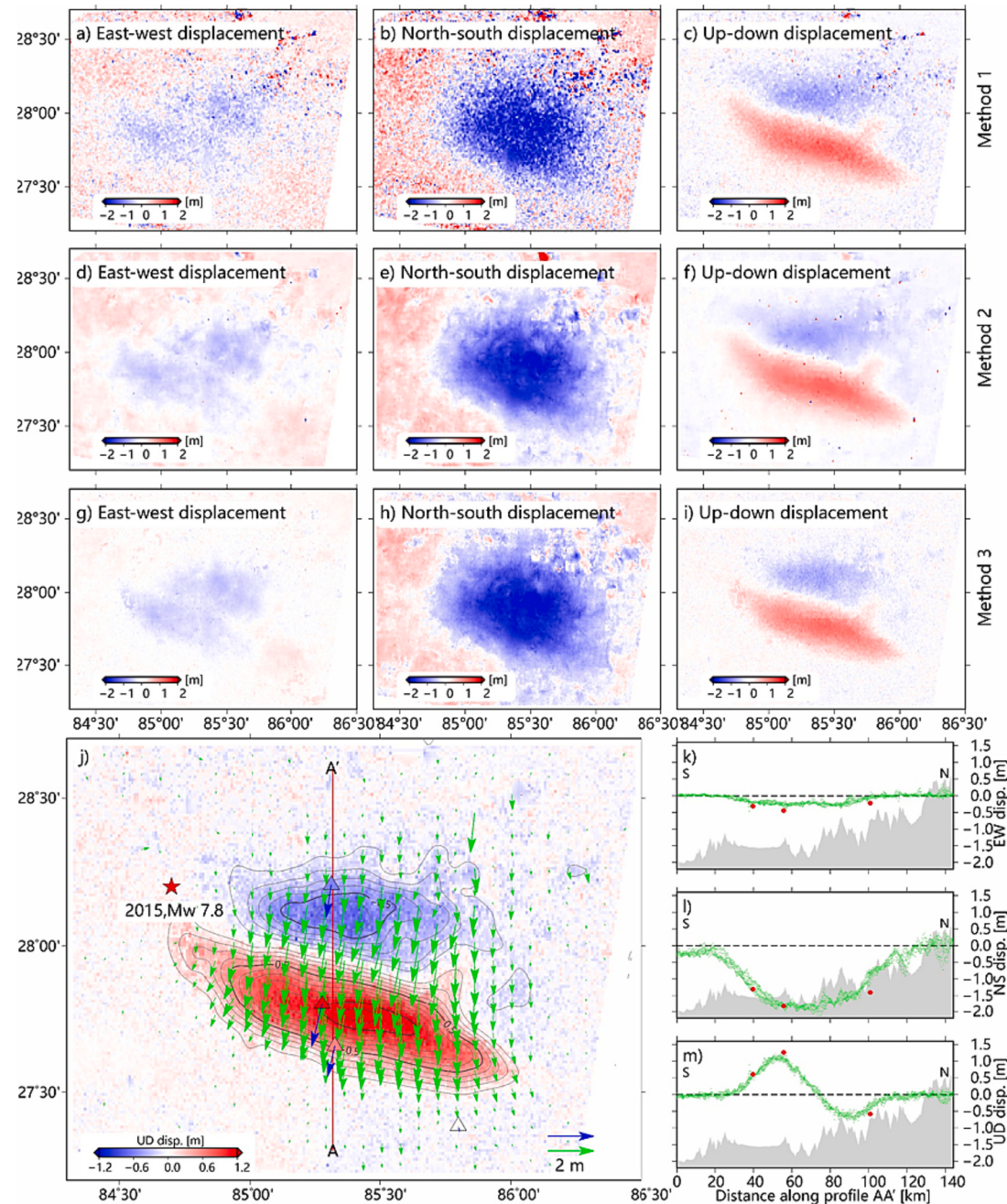


**Fig. 3.** The resolved 3-D displacement fields of the Gorkha earthquake using three methods. (a, d, g) East-west displacements. (b, e, h) North-south displacements. (c, f, i) Vertical displacements. (j, k, l, m) Comparison between 3-D displacements and GPS observations. (j) The colored background indicates the vertical deformation, and the green arrows denote the horizontal displacements. Colored triangles and blue arrows illustrate vertical and horizontal components of GPS displacement. (k, l, m) Comparison between our derived (green dots) and GPS-observed (red dots) 3-D components. (For interpretation of the references to colour in this figure legend, the reader is referred to the web version of this article.)

window dimensions (Fig. S2a). The amplitude difference between them, shown in Fig. S2b, was  $<0.5$  m. Notably, pixels exhibiting larger amplitude differences also presented increased standard deviations, indicative of potential mismatches or errors rather than reliable offset measurements (Figs. S2b, S2c). We conclude that Sentinel-1 azimuth offsets in our subsequent 3-D displacement reconstruction are reliable using the adopted filter strength and the matching window size.

### 3.2. 3-D coseismic displacement fields

We used three methods to reconstruct the 3-D coseismic displacements. The results, derived from three methods, and their differences are displayed in Figs. 3 and S3. In Method 1, we use three LOS and three azimuth offset measurements (Fig. 2) to directly invert 3-D displacements as outlined in Wright et al. (2004). In Method 2, we incorporate the strain model proposed in Section 2.3 (Liu et al., 2018). In Method 3, we adopt the strain model in a Bayesian framework (Section 2.3).

Overall, the results from the three methods depict similar 3-D displacement patterns. The similar pattern between the resolved north-south displacements (Fig. 3) and the azimuth offsets (Fig. 2) attest to the key constraints on north-south displacement from azimuth offsets. Method 1 cannot well determine the north-south displacements, which heavily relies on the quality of azimuth offsets (i.e., speckle noise level; Figs. 3, S3). The implemented strain model in methods 2 and 3 can eliminate low-quality pixels with high speckle noise levels in Sentinel-1 azimuth offsets. This is because the strain model considered the spatial correlation between adjacent points, which helps to suppress the speckle noise in azimuth offsets. As a result, methods 2 and 3 provide better constraints on north-south displacements. We evaluate the methods 2 and 3 using two standards: (1) the match between the resolved 3-D displacements and independent 3-D coseismic GPS displacements; (2) root-mean-square (RMS) between InSAR observations and model calculations. The RMS is calculated using the following equation:

$$RMS = \sqrt{\frac{\sum_{i=1}^n (D_{obs}^i - D_{model}^i)^2}{n}}$$

where  $D_{obs}^i$  is observations,  $D_{model}^i$  is model calculations,  $n$  is the number of observations.

We calculated the mean resolved 3-D displacements within a 5 km radius of each GPS site and then determined their deviation from the 3-D coseismic GPS displacements. The results reveal a lower mean mismatch for Method 3 (0.152 m) compared to Method 2 (0.184 m), demonstrating Method 3 superior accuracy in matching coseismic 3-D GPS displacements. For Method 3, the RMS errors for LOS displacements were 0.088 and 0.074 for the two Sentinel-1 datasets, and 0.104 for the ALOS-2 dataset. For azimuth displacements, the RMS errors were 1.282 and 1.348 for the Sentinel-1 datasets, and 0.296 for the ALOS-2 dataset. For Method 2, the RMS for LOS displacements were 0.402 and 0.211 for the two Sentinel-1 datasets, respectively, and 0.200 for the ALOS-2 dataset. The RMS errors for azimuth displacements were 1.212 and 1.232 for the Sentinel-1 datasets, and 0.344 for the ALOS-2 dataset (Fig. S4, S5). Method 3 demonstrates a significantly smaller RMS for all LOS displacements and the azimuth displacement of ALOS-2 data, compared to Method 2. However, for the azimuth displacements of Sentinel-1 data, Method 2 exhibits a lower RMS than Method 3. Given the higher noise levels in the azimuth displacements of Sentinel-1 data, the larger RMS observed with Method 3 may suggest a closer approximation to the actual values. The observed variation in RMS between Method 2 and Method 3 highlights a potential trade-off in Method 3's weighting across different datasets. While we applied equal weighting (1:1) for all LOS measurements and azimuth offsets in our study, method 3 shows a preference for fitting data with lower noise levels more accurately instead of noisier datasets. Our preference for the 3-D decomposing results by Method 3 stems from its best match with

independent 3-D coseismic GPS displacements and the minimum RMS misfits for all LOS displacement measurements (Fig. S4) and the azimuth offset data from ALOS-2 (Fig. S5). Method3's efficacy is particularly noteworthy as it achieves these results without necessitating additional adjustments for data weighting across various datasets.

Fig. 3j-3m demonstrates the resolved 3-D displacements and its comparison to coseismic GPS displacements (Wang and Fialko, 2015). Two narrow zones of uplift deformation to the south and subsidence deformation to the north are identified in the 3-D displacement field, in accordance with the thrust motion of the MHT. The amplitude of coseismic uplift is  $\sim 1.1$  m, slightly larger than the subsidence. The east-west motion pattern contrasts with the conventional four-quadrant distribution observed in the results of Elliott et al. (2016). In our study, we observe primarily westward deformation, which is consistent with the results reported by Qu et al. (2020). The amplitude of this westward motion is  $\sim 0.5$  m. The north-south motion is characterized by deformation to the south with an amplitude of  $\sim 2$  m, consistent with previous studies (Elliott et al., 2016; Qu et al., 2020). Overall, our derived 3-D displacements match the GPS observations well. Slight discrepancy between our derived and GPS-observed 3-D displacements may result from diverse resolutions of GPS/InSAR data, the azimuth offset amplitude reduction during the filtering, minor postseismic deformation and/or atmospheric phase noise contained in InSAR measurements. The corresponding uncertainties of our derived 3-D displacements by Method 3 are shown in Figs. S6, S7. For the north-south and vertical displacements, the uncertainty is mostly  $<0.5$  m, suggesting the robustness of our results.

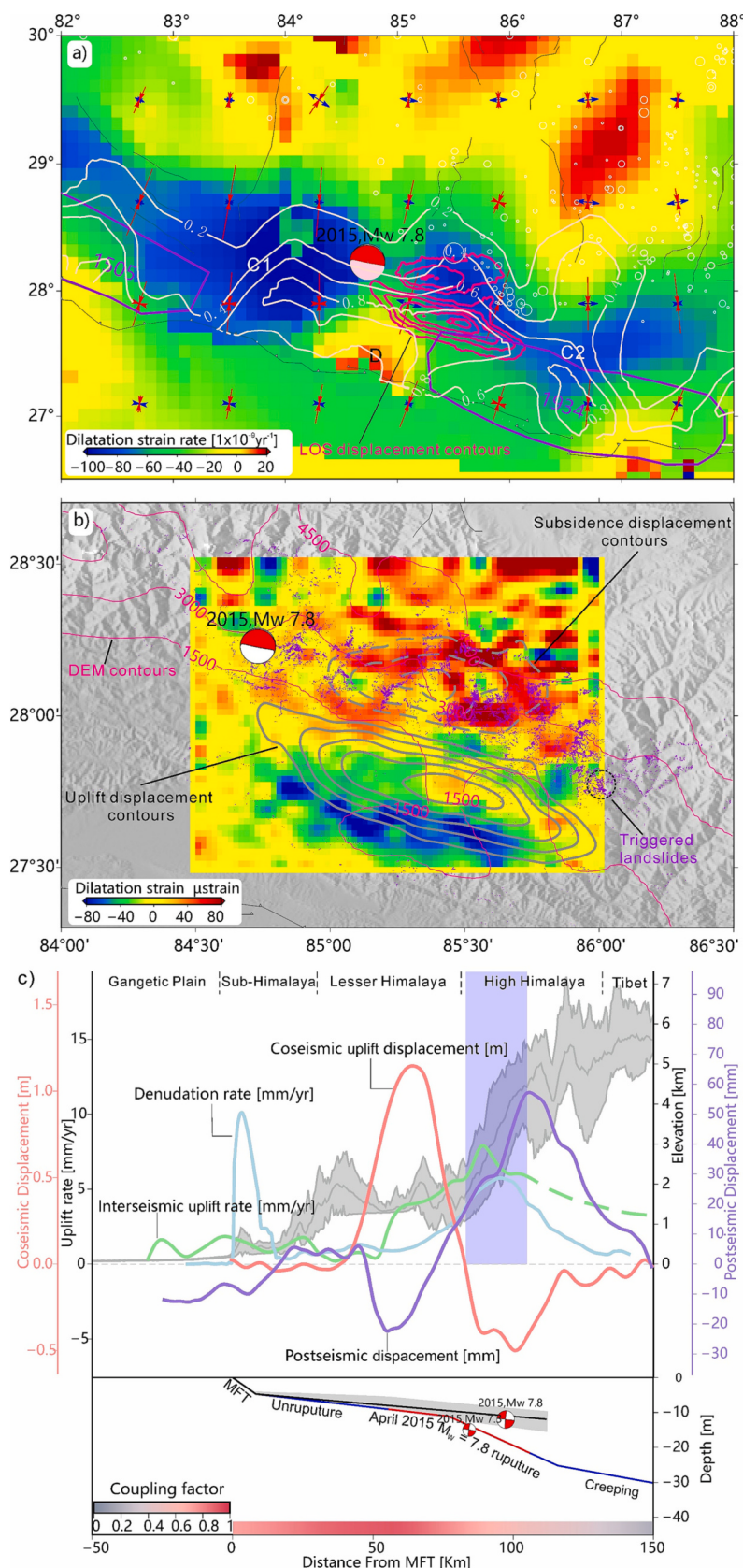
## 4. Discussion

### 4.1. Interseismic strain

Interseismic strain rate along the fault depicts the distribution and the accumulation of tectonic strain, likely relating to the stress build-up before the next large earthquake. In this section, we illustrate the spatial relationship between the interseismic dilatational strain rate and the 2015 Gorkha earthquake by computing the interseismic strain rate using the interseismic GPS datasets by Wang and Shen (2020). For a detailed data description and calculation of the interseismic strain rate, readers are referred to Text S2.

GPS-based interseismic strain rate is highly sensitive to the spatial distribution and density of GPS stations (e.g., Wang and Shen, 2020). To assess the impact of station density on the distribution and magnitude of the strain rate, we varied GPS station densities in the calculation (Fig. S8a-S8e). The results indicate that decreasing GPS station density makes the interseismic strain rate smoother, revealing only the first-order pattern and fewer details. Overall, the notable band of the contraction strain with varied width ( $<-70$  nano-strain per year) is parallel to the Himalayan belt, which is due to the interseismic locking of the MHT (Figs. 1, 4). Spatially, the interseismic dilatational strain transitions from the dominant contraction near the MHT and Higher Himalayas to the extensional strain toward the southern Tibetan Plateau. Locally, the dilatational strain rate reveals two distinct areas of contraction deformation: a smaller patch to the east and a larger one to the west of the source region of the Gorkha earthquake (Fig. 4). The eastern contraction region (C2 area in Fig. 4a) is the ruptured part during the Gorkha earthquake, and the western contraction region (C1 area in Fig. 4a) is argued to have a high seismic potential for generating a large future earthquake (e.g., Sreejith et al., 2018).

To the south of the source region of the Gorkha earthquake, we observe an abnormal dilatation region (marked as 'D' in Fig. 4a). Our test (Fig. S8f) of discarding one GPS site in this region leads us to conclude that the observed dilatation is biased because the dilatation signal highly depends on one GPS site near the Gorkha earthquake. We speculate the GPS interseismic velocity field might still contain residual coseismic and postseismic deformations of the Gorkha earthquake due



(caption on next page)

**Fig. 4.** (a) Comparison of interseismic dilatational strain rate from GPS measurements (Wang and Shen, 2020), historical rupture extent (purple polygons), interseismic coupling (beige contour lines; Dal Zilio et al., 2020) and InSAR LOS displacements of the Gorkha earthquake (red contour lines). (b) Spatial distribution of coseismic dilatational strain, coseismic deformation (dashed grey contours: subsidence, grey contours: uplift), and triggered landslides (purple dots, from Roback et al., 2018). The pink contours show elevation variations. (c) Cross-section ( $N15^{\circ}$  E) across central Nepal showing topography, tectonic uplift, denudation rate, and the geometries of the MHT fault. Upper panel: The shaded grey area shows elevation variations along the profile. The light green line is the interseismic uplift rate from leveling data (Grandin et al., 2012). The light red line is the coseismic uplift displacement from 3-D displacement decomposing in this study. The light purple line is postseismic LOS displacement from InSAR data, processed by Wang and Fialko, (2018). The shaded purple area indicates the major landslide areas (Roback et al., 2018). Lower panel: The black line is the denudation rate, from Grandin et al. (2012). The blue line is the MHT with a mid-crustal ramp (Herman et al., 2010), and the red part is the Gorkha earthquake rupture area. The colored ribbon shows the interseismic coupling of the MHT (Dal Zilio et al., 2020). (For interpretation of the references to colour in this figure legend, the reader is referred to the web version of this article.)

to the imperfect modeling in Wang and Shen (2020). Given the similar levels of interseismic locking around the Gorkha earthquake, it seems unlikely that the area around the earthquake's epicenter would experience relatively lower contraction strain (Fig. 4a, Dal Zilio et al., 2020). We speculate that this could also be due to the influence of coseismic and postseismic residual deformations associated with the Gorkha earthquake. Overall, the width of the contraction zone between  $83^{\circ}$ E and  $87^{\circ}$ E longitude is consistent with the width of the interseismic locking zone (coupling ratio  $> 0.5$ ; Dal Zilio et al., 2020). We conclude that the 2015 Gorkha region's source region (with 3-D coseismic displacements resolved in this study) is experiencing the contraction strain during the interseismic period.

#### 4.2. Possible relationship between coseismic strain and triggered landslides

The occurrence of landslides triggered by the 2015 Gorkha earthquake highlights the complex interplay of geological, topographical, and seismic factors (Meunier et al., 2007; García-Rodríguez et al., 2008; Owen et al., 2008; Shen et al., 2016). Although steep slopes have been traditionally considered a primary factor for landslides (Gorum et al., 2011; Liu and Wang, 2023), the pattern of landslide distribution during the earthquake challenges this assumption. Research by Roback et al. (2018) shows that areas with the steepest slopes did not correspond with the highest landslide density. Instead, many landslides occurred in areas with relatively gentle slopes, indicating that other factors also play a significant role.

Elliott et al. (2016) and Kohn et al. (2004) provide critical insights into the geological and topographical dynamics of the Himalayan region affected by the earthquake. They highlight the role of in-sequence thrusting and the southward propagation of the Main Himalayan Thrust (MHT), which has led to an evolving landscape that may be more prone to landslides, even in areas of gentler slopes. This evolving topography, along with factors such as lithology and seismic shaking, contributes to landslide susceptibility.

Xu et al. (2016) further emphasize that the dynamics of landslides are influenced by a combination of factors, including the lithology and the slope of the mountains, beyond the simple equation of steeper equals more dangerous. This view is supported by the analysis of seismic factors, where the distribution of landslides during the Gorkha earthquake did not show a high correlation with Peak Ground Acceleration (PGA), suggesting a more complex causation mechanism (Roback et al., 2018).

Our study focuses on the spatial correlation between coseismic subsidence and landslides, contrasting with areas of coseismic uplift. We find that extensional strain, primarily found in areas of coseismic subsidence, is closely associated with landslide occurrences, with over 80% of landslides located in regions experiencing extensional strain. This correlation is statistically significant, as confirmed by a chi-squared test with a high chi-squared value and a  $P$ -value of  $<0.01$  (Details in Text S3). Lavé and Avouac (2000) discuss the long-term denudation rates in these regions, suggesting that prolonged erosional forces contribute to the weakening of material shear strength. This weakening, coupled with the seismic extensional strain, decreases the shear strength of materials, increasing the likelihood of landslides during seismic events.

In conclusion, our analysis confirms that a complex set of factors, including slope, rock rheology, dynamic shaking, and coseismic extensional strain, collectively contribute to the conditions conducive to landslides during major earthquakes. This comprehensive approach challenges the oversimplified view that steep slopes are the primary trigger for landslides, underscoring the importance of considering multiple factors in landslide risk assessment.

#### 4.3. Earthquake cycle deformation of MHT

Earthquake cycle deformation and the geometry of the MHT remain central to the improved understanding of the long-term mountain build process. Deformation over the entire earthquake cycle, whether transient and elastic or permanent and inelastic (coseismic, postseismic and interseismic) is controlled by the fault geometry and physical properties of the fault (Avouac, 2003; Avouac et al., 2015; Diao et al., 2021). The elastic deformation is produced by the tectonic motion of the active thrust faults and the inelastic deformation is mainly accommodated by the pervasive folds, accretion and erosion processes along the Himalaya (Avouac, 2003). The distinct portions of locked or slipped areas along the MHT's dip direction during earthquake cycles result in a surface deformation pattern with diverse characteristics (Fig. 4c).

During the interseismic period, the Main Himalayan Thrust (MHT) exhibits distinct behaviours in its different segments. The upper, locked portion of the MHT maintains elastic strain, while the deeper segment undergoes steady creep. This contrast in movement, particularly the gently dipping geometry of the deeper portion, results in transient uplift in the transition zone. Notably, the highest observed uplift velocity at the Annapurna Mountain range front, estimated at approximately 7 mm/year, was recorded by InSAR between 2003 and 2010 in west-central Nepal (Grandin et al., 2012). This measurement aligns with peak uplift velocities derived from leveling data near Kathmandu (Jackson and Bilham, 1994; Fig. 4c).

During seismic events, the previously interseismically locked segment of the MHT ruptures. This leads to uplift in the southern region above the fault slip area and corresponding subsidence in the northern region. Our refined 3-D displacement analysis, as presented in Fig. 3, reveals a peak uplift displacement of around 1.1 m. This displacement closely correlates with the deep fault slip region (Elliott et al., 2016) and is matched by the largest subsidence, approximately 0.7 m, in the northern area during the Gorkha earthquake.

In the aftermath of the earthquake, geodetic studies have observed time-dependent postseismic deformation. However, this deformation is predominantly confined to the coseismic rupture area and the downdip portion of the fault (e.g., Diao et al., 2021; Liu-Zeng et al., 2020; Wang and Fialko, 2018). The Line of Sight (LOS) displacement, characterized by an amplitude of roughly 70 mm over two years following the 2015 Gorkha earthquake (Wang and Fialko, 2018), exhibits an uplift and subsidence pattern nearly opposite to that observed during the coseismic phase. The significant subsidence in the Kathmandu basin, primarily viewed as a non-tectonic signal, is likely attributable to extensive water pumping in Kathmandu (Wang and Fialko, 2018; Hong and Liu, 2021). In contrast, the uplift observed is mainly driven by afterslip along the downdip extension of the MHT. This suggests that motion akin to the

coseismic displacement occurs further north of the coseismic rupture zone, leading to a reversed deformation pattern at the Earth's surface in the same area. It is crucial to note that during both the coseismic and postseismic phases, the up-dip region of the MHT experiences little significant slip. However, this region undergoes stress transfer from both coseismic slip and afterslip, potentially accumulating enough strain to trigger future earthquakes (Mencin et al., 2016).

Overall, the interseismic vertical displacements show an overall uplift pattern but mainly contribute to the transition area of Lesser Himalaya and High Himalaya. The postseismic (dominated by deep afterslip after the Gorkha earthquake) LOS displacement profile is spatially complementary with the coseismic vertical displacements (Fig. 4c). As the Gorkha earthquake, characterized by a partial rupture, failed to reach the surface, it does not represent a typical characteristic earthquake, the estimated coseismic uplift deformation is indeed atypical and has limitations to extrapolate over multiple earthquake cycles. The net uplift over earthquake cycles depends on the earthquake recurrence interval in that region, which is largely unknown (Bilham, 2019). Considering these factors, it is important to acknowledge that conducting quantitative studies on earthquake cycles in this region can be challenging. Addressing these challenges may require the acquisition of additional data and further research efforts in the future.

## 5. Conclusions

In this study, we systematically analyze all available coseismic InSAR datasets to explore the 3-D displacement fields of the Gorkha earthquake. We rigorously evaluate three methods for resolving the 3-D coseismic displacements, demonstrating that azimuth offsets and the strain model, within a Bayesian framework, are particularly effective in constraining the north-south displacement component. This analysis reveals a pattern in vertical deformation that closely aligns with the Line of Sight (LOS) displacement, highlighting a maximum uplift of approximately 1.1 m. This uplift slightly exceeds the observed coseismic subsidence, underscoring the dynamic nature of the earthquake's impact.

Our findings indicate that the Gorkha earthquake has played a significant role in partially releasing the accumulated interseismic strain along the Main Himalayan Thrust (MHT). This observation is crucial, as it suggests that significant seismic hazards persist in the vast region surrounding western Nepal. Furthermore, our study unveils that over 80% of landslides occur in zones marked by significant coseismic extensional strain and steep slopes. Notably, these areas correspond spatially with regions of long-term denudation, implying a strong link between seismic activity and landscape evolution.

The diverse tectonic uplift processes observed during earthquake cycles contribute distinctly to long-term mountain building. In this context, the Gorkha earthquake serves as a pivotal case study, revealing that the patterns of interseismic and postseismic uplift are in stark contrast to those observed during coseismic rupture. This finding is instrumental in understanding the complex interplay between seismic events and mountain formation processes. Consequently, this study not only advances our comprehension of earthquake-induced landscape changes but also emphasizes the need for ongoing vigilance in earthquake-prone regions, particularly in the context of hazard assessment and land-use planning.

## Data and resources

The Sentinel-1A/B Synthetic Aperture Radar data were acquired by the European Space Agency (ESA) and distributed by Alaska Satellite Facility (<https://search.asf.alaska.edu/>), and Advanced Land Observing Satellite 2 (ALOS-2) data is available via contract with PASCO Corporation. Historical seismicity used in this study can be obtained from the China Earthquake Networks Center (<https://news.ceic.ac.cn/>). Focal mechanisms used in this study can be obtained from the Global Centroid Moment Tensor Project at [www.globalcmt.org](http://www.globalcmt.org) (last accessed November

2021). The supplemental material for this article includes three texts, one table, and eight figures.

## CRediT authorship contribution statement

**Han Chen:** Writing – original draft, Visualization, Validation, Methodology, Investigation, Data curation. **Chunyan Qu:** Supervision, Resources, Investigation, Funding acquisition, Conceptualization. **Dezheng Zhao:** Writing – review & editing, Writing – original draft, Methodology, Conceptualization. **Xinjian Shan:** Funding acquisition. **Chao Ma:** Supervision, Conceptualization. **Wenyu Gong:** Methodology. **Lei Zhao:** Methodology, Data curation. **Luca Dal Zilio:** Writing – review & editing, Data curation.

## Declaration of competing interest

The authors acknowledge that there are no conflicts of interest recorded.

## Data availability

Data will be made available on request.

## Acknowledgements

We would like to thank the European Space Agency and Japan Aerospace Exploration Agency for providing Sentinel-1A/B and ALOS-2 data, Raphaël Grandin for providing leveling data, and Cunren Liang for providing azimuth deformation of the ALOS-2 data. This work was supported by the Basic Scientific Funding of the Institute of Geology, China Earthquake Administration (IGCEA1809, IGCEA2104), and the National Natural Science Foundation of China (42174009, 42374007). Figures were prepared using the public domain Generic Mapping Tools (GMT, Wessel et al., 2013). Luca Dal Zilio was supported by the European Research Council (ERC) Synergy Grant “Fault Activation and Earthquake Rupture” (FEAR) (No 856559), the EU project “A Digital Twin for Geophysical Extremes” (DT-GEO) (No 101058129).

## Appendix A. Supplementary data

Supplementary data to this article can be found online at <https://doi.org/10.1016/j.tecto.2024.230254>.

## References

- Avouac, J.P., 2003. Mountain building, erosion, and the seismic cycle in the Nepal Himalaya. *Adv. Geophys.* 46, 1–80.
- Avouac, J.P., 2015. Mountain building: from earthquakes to geologic deformation. *Treat. Geophys.* 381–432.
- Avouac, J.P., Meng, L., Wei, S., Wang, T., Ampuero, J.P., 2015. Lower edge of locked Main Himalayan Thrust unzipped by the 2015 Gorkha earthquake. *Nat. Geosci.* 8 (9), 708–711.
- Bamler, R., Eineder, M., 2005. Accuracy of differential shift estimation by correlation and split-bandwidth interferometry for wideband and delta-k SAR systems. *IEEE Geosci. Remote Sens. Lett.* 2 (2), 151–155.
- Bilham, R., 2019. Himalayan earthquakes: a review of historical seismicity and early 21st century slip potential. *Geol. Soc. Lond. Spec. Publ.* 483 (1), 423–482.
- Chuang, R.Y., Lu, C.H., Yang, C.J., Lin, Y.S., Lee, T.Y., 2020. Coseismic uplift of the 1999 Mw7.6 Chi-Chi earthquake and implication to topographic change in frontal mountain belts. *Geophys. Res. Lett.* 47 (15), e2020GL088947.
- Dal Zilio, L., van Dinther, Y., Gerya, T., Avouac, J.P., 2019. Bimodal seismicity in the Himalaya controlled by fault friction and geometry. *Nat. Commun.* 10 (1), 48.
- Dal Zilio, L., Jolivet, R., van Dinther, Y., 2020. Segmentation of the Main Himalayan Thrust illuminated by Bayesian inference of interseismic coupling[J]. *Geophys. Res. Lett.* 47 (4), e2019GL086424.
- Dal Zilio, L., Hetényi, G., Hubbard, J., Bollinger, L., 2021. Building the Himalaya from tectonic to earthquake scales. *Nat. Rev. Earth Environ.* 2 (4), 251–268.
- Diao, F., Wang, R., Xiong, X., Liu, C., 2021. Overlapped postseismic deformation caused by afterslip and viscoelastic relaxation following the 2015 Mw 7.8 Gorkha (Nepal) earthquake. *J. Geophys. Res. Solid Earth* 126 (3), e2020JB020378.

- Elliott, J.R., Jolivet, R., González, P.J., Avouac, J.P., Hollingsworth, J., Searle, M.P., Stevens, V.L., 2016. Himalayan megathrust geometry and relation to topography revealed by the Gorkha earthquake. *Nat. Geosci.* 9 (2), 174–180.
- Feng, G., Li, Z., Shan, X., Zhang, L., Zhang, G., Zhu, J., 2015. Geodetic model of the 2015 April 25 M w 7.8 Gorkha Nepal Earthquake and M w 7.3 aftershock estimated from InSAR and GPS data. *Geophys. J. Int.* 203 (2), 896–900.
- García-Rodríguez, M.J., Malpica, J.A., Benito, B., Díaz, M., 2008. Susceptibility assessment of earthquake-triggered landslides in El Salvador using logistic regression. *Geomorphology* 95 (3–4), 172–191.
- Goodman, J., Weare, J., 2010. Ensemble samplers with affine invariance. *Commun. Appl. Math. Comput. Sci.* 5 (1), 65–80.
- Gorum, T., Fan, X., van Westen, C.J., et al., 2011. Distribution pattern of earthquake-induced landslides triggered by the 12 May 2008 Wenchuan earthquake[J]. *Geomorphology* 133 (3–4), 152–167.
- Grandin, R., Doin, M.P., Bollinger, L., Pinel-Puysségur, B., Ducret, G., Jolivet, R., Sapkota, S.N., 2012. Long-term growth of the Himalaya inferred from interseismic InSAR measurement. *Geology* 40 (12), 1059–1062.
- Gudmundsson, S., Sigmundsson, F., Carstensen, J.M., 2002. Three-dimensional surface motion maps estimated from combined interferometric synthetic aperture radar and GPS data. *J. Geophys. Res. Solid Earth* 107 (B10), ETG-13.
- Herman, F., Copeland, P., Avouac, J.P., et al., 2010. Exhumation, crustal deformation, and thermal structure of the Nepal Himalaya derived from the inversion of thermochronological and thermobarometric data and modeling of the topography [J]. *J. Geophys. Res. Solid Earth* 115 (B6).
- Hong, S., Liu, M., 2021. Postseismic deformation and afterslip evolution of the 2015 Gorkha earthquake constrained by InSAR and GPS observations. *J. Geophys. Res.: Solid Earth* 126 (7), e2020JB020230.
- Hu, J., Li, Z.W., Ding, X.L., Zhu, J.J., Zhang, L., Sun, Q., 2014. Resolving three-dimensional surface displacements from InSAR measurements: a review. *Earth Sci. Rev.* 133, 1–17.
- Ingleby, T., Wright, T.J., Hooper, A., Craig, T.J., Elliott, J.R., 2020. Constraints on the geometry and frictional properties of the Main Himalayan Thrust using coseismic, postseismic, and interseismic deformation in Nepal. *J. Geophys. Res. Solid Earth* 125 (2), e2019JB019201.
- Jackson, M., Bilham, R., 1994. Constraints on Himalayan deformation inferred from vertical velocity fields in Nepal and Tibet. *J. Geophys. Res. Solid Earth* 99 (B7), 13897–13912.
- Kohn, M.J., Wieland, M.S., Parkinson, C.D., Upadhyay, B.N., 2004. Miocene faulting at plate tectonic velocity in the Himalaya of Central Nepal. *Earth Planet. Sci. Lett.* 228 (3–4), 299–310.
- Lavé, J., Avouac, J.P., 2000. Active folding of fluvial terraces across the Siwaliks Hills, Himalayas of Central Nepal. *J. Geophys. Res. Solid Earth* 105 (B3), 5735–5770.
- Liang, C., Fielding, E.J., 2017. Measuring azimuthal deformation with L-band ALOS-2 ScanSAR interferometry. *IEEE Trans. Geosci. Remote Sens.* 55 (5), 2725–2738.
- Lindsey, E.O., Natsukawa, R., Xu, X., et al., 2015. Line-of-sight displacement from ALOS-2 interferometry: Mw 7.8 Gorkha Earthquake and Mw 7.3 aftershock[J]. *Geophys. Res. Lett.* 42 (16), 6655–6661.
- Liu, J.H., Hu, J., Li, Z.W., Zhu, J.J., Sun, Q., Gan, J., 2018. A method for measuring 3-D surface deformations with InSAR based on strain model and variance component estimation. *IEEE Trans. Geosci. Remote Sens.* 56 (1), 239–250.
- Liu, R., Wang, T., 2023. The relationship between three-dimensional coseismic displacement and distribution of coseismic landslides[J]. *Sci. China Earth Sci.* 1–20.
- Liu-Zeng, J., Zhang, Z., Rollins, C., Gualandi, A., Avouac, J.P., Shi, H., Wang, P., Chen, W., Zhang, R., Zhang, P., Wang, W., Li, Y., Wang, T., Li, Z., Li, Z., 2020. Postseismic deformation following the 2015 Mw7.8 Gorkha (Nepal) earthquake: new GPS data, kinematic and dynamic models, and the roles of afterslip and viscoelastic relaxation. *J. Geophys. Res. Solid Earth* 125 (9), e2020JB019852.
- Mahmoud, A.M.A., Novellino, A., Hussain, E., et al., 2020. The use of SAR offset tracking for detecting sand dune movement in Sudan[J]. *Remote Sens.* 12 (20), 3410.
- Mencin, D., Bendick, R., Upadhyay, B.N., Adhikari, D.P., Gajurel, A.P., Bhattacharai, R.R., Shrestha, H.R., Bhattacharai, T.N., Manandhar, N., Galetzka, J., Knappe, E., Pratt-Sitaula, B., Aoudia, A., Bilham, R., 2016. Himalayan strain reservoir inferred from limited afterslip following the Gorkha earthquake. *Nat. Geosci.* 9 (7), 533–537.
- Mendoza, M.M., Ghosh, A., Karplus, M.S., Klempner, S.L., Sapkota, S.N., Adhikari, L.B., Velasco, A., 2019. Duplex in the Main Himalayan Thrust illuminated by aftershocks of the 2015 M w 7.8 Gorkha earthquake. *Nat. Geosci.* 12 (12), 1018–1022.
- Meunier, P., Hovius, N., Haines, A.J., 2007. Regional patterns of earthquake-triggered landslides and their relation to ground motion. *Geophys. Res. Lett.* 34 (20).
- Owen, L.A., Kamp, U., Khattak, G.A., Harp, E.L., Keefer, D.K., Bauer, M.A., 2008. Landslides triggered by the 8 October 2005 Kashmir earthquake. *Geomorphology* 94 (1–2), 1–9.
- Qiu, Q., Hill, E.M., Barbot, S., Hubbard, J., Feng, W., Lindsey, E.O., Feng, L., Dai, K., Samsonov, S.V., Tapponnier, P., 2016. The mechanism of partial rupture of a locked megathrust: the role of fault morphology. *Geology* 44 (10), 875–878.
- Qu, C., Qiao, X., Shan, X., Zhao, D., Zhao, L., Gong, W., Li, Y., 2020. InSAR 3-D coseismic displacement field of the 2015 Mw 7.8 Nepal earthquake: insights into complex fault kinematics during the event. *Remote Sens.* 12 (23), 3982.
- Roback, K., Clark, M.K., West, A.J., Zekkos, D., Li, G., Gallen, S.F., Chamlagain, D., Godt, J.W., 2018. The size, distribution, and mobility of landslides caused by the 2015 Mw7.8 Gorkha earthquake, Nepal. *Geomorphology* 301, 121–138.
- Shen, L., Xu, C., Liu, L., 2016. Interaction among controlling factors for landslides triggered by the 2008 Wenchuan, China Mw 7.9 earthquake. *Front. Earth Sci.* 10, 264–273.
- Sreejith, K.M., Sunil, P.S., Agrawal, R., Saji, A.P., Ramesh, D.S., Rajawat, A.S., 2016. Coseismic and early postseismic deformation due to the 25 April 2015, Mw 7.8 Gorkha, Nepal, earthquake from InSAR and GPS measurements. *Geophys. Res. Lett.* 43 (7), 3160–3168.
- Sreejith, K.M., Sunil, P.S., Agrawal, R., Saji, A.P., Rajawat, A.S., Ramesh, D.S., 2018. Audit of stored strain energy and extent of future earthquake rupture in central Himalaya. *Sci. Rep.* 8 (1), 1–9.
- Strozzi, T., Luckman, A., Murray, T., et al., 2002. Glacier motion estimation using SAR offset-tracking procedures[J]. *IEEE Trans. Geosci. Remote Sens.* 40 (11), 2384–2391.
- Tung, S., Masterlark, T., 2016. Coseismic slip distribution of the 2015 Mw7.8 Gorkha, Nepal, earthquake from joint inversion of GPS and InSAR data for slip within a 3-D heterogeneous domain. *J. Geophys. Res. Solid Earth* 121 (5), 3479–3503.
- Wang, C., Chang, L., Wang, X.S., Zhang, B., Stein, A., 2024. Interferometric synthetic aperture radar statistical inference in deformation measurement and geophysical inversion: a review. *IEEE Geosci. Remote Sens.* 56 (1), 239–250.
- Wang, K., Fialko, Y., 2015. Slip model of the 2015 Mw 7.8 Gorkha (Nepal) earthquake from inversions of ALOS-2 and GPS data. *Geophys. Res. Lett.* 42 (18), 7452–7458.
- Wang, K., Fialko, Y., 2018. Observations and modeling of coseismic and postseismic deformation due to the 2015 Mw 7.8 Gorkha (Nepal) earthquake. *J. Geophys. Res. Solid Earth* 123 (1), 761–779.
- Wang, M., Shen, Z.K., 2020. Present-day crustal deformation of continental China derived from GPS and its tectonic implications. *J. Geophys. Res. Solid Earth* 125 (2), e2019JB018774.
- Werner, C., Wegmüller, U., Strozzi, T., Wiesmann, A., 2005, July. Precision estimation of local offsets between pairs of SAR SLCs and detected SAR images. In: International Geoscience and Remote Sensing Symposium, vol. 7, p. 4803.
- Wessel, P., Smith, W.H., Scharroo, R., Luis, J., Wobbe, F., 2013. Generic mapping tools: improved version released. *EOS Trans. Am. Geophys. Union* 94 (45), 409–410.
- Whipple, K.X., Shirzaei, M., Hodges, K.V., Arrowsmith, J.R., 2016. Active shortening within the Himalayan orogenic wedge implied by the 2015 Gorkha earthquake. *Nat. Geosci.* 9 (9), 711–716.
- Wright, T.J., Parsons, B.E., Lu, Z., 2004. Toward mapping surface deformation in three dimensions using InSAR. *Geophys. Res. Lett.* 31 (1).
- Xu, C., Xu, X., Tian, Y., et al., 2016. Two comparable earthquakes produced greatly different coseismic landslides: the 2015 Gorkha, Nepal and 2008 Wenchuan, China events. *J. Earth Sci.* 27 (6), 1008–1015.
- Yagüe-Martínez, N., Prats-Iraola, P., Gonzalez, F.R., et al., 2016. Interferometric processing of Sentinel-1 TOPS data. *IEEE Trans. Geosci. Remote Sens.* 54 (4), 2220–2234.
- Yue, H., Simons, M., Duputel, Z., Jiang, J., Fielding, E., Liang, C., Owen, S., Moore, A., Riel, B., Ampuero, J.P., Samsonov, S., Samsonov, S.V., 2017. Depth varying rupture properties during the 2015 Mw 7.8 Gorkha (Nepal) earthquake. *Tectonophysics* 714, 44–54.
- Zhao, B., Bürgmann, R., Wang, D., Tan, K., Du, R., Zhang, R., 2017. Dominant controls of downdip afterslip and viscous relaxation on the postseismic displacements following the Mw7.9 Gorkha, Nepal, earthquake. *J. Geophys. Res. Solid Earth* 122 (10), 8376–8401.